This article has been accepted for publication in a future issue of this journal, but has not been fully edited. Content may change prior to final publication.
Citation information: DOI: 10.1109/TPEL.2026.3674121,

Analytical Characterization of Grid-Forming Converter Response Time Under Voltage Sags

Minshen Lin, Li Zhang, *Senior Member, IEEE*, Qichen Yang,
Diaa-Eldin A. Mansour, *Senior Member, IEEE*, and Ahmed F. Zobaa, *Senior Member, IEEE*

***Abstract*—The response time of grid-forming (GFM) converters under grid disturbances is a critical metric that reflects how fast GFM capabilities can be delivered. In this letter, the analytical expression for the response time under voltage sags is derived using the geometric singular perturbation method. It is revealed that the response speed is naturally faster in weaker grids, and for a wide range of grid conditions, the response time under voltage sags has an inherent minimum limit of a quarter of the fundamental cycle, i.e., 5 ms at 50 Hz. Increasing the voltage-loop integral gain k_{iv} approaches this limit, but an excessively large k_{iv} induces small-signal instability. Hence, a transient reactive current augmentation strategy is proposed to approach and even break the limit while ensuring stability. Moreover, it is derived that current-limiting control reduces the response time. Therefore, the analytical response time constitutes an upper bound on the practical response time with current limiting. The findings suggest potential refinements to grid code requirements for GFM converter response time. The results are validated by hardware-in-the-loop testing.**

***Index Terms*—Grid forming control, response time, voltage sag**

I. Introduction

As power systems transition toward high shares of inverter-based resources, system strength and voltage stiffness decline, challenging the stable operation of grid-following converters. Grid-forming (GFM) converters have therefore emerged as a promising solution by forming both frequency and voltage to support the stable operation of weak grids. Beyond stability, grid codes are evolving to specify GFM capability requirements during grid disturbances [1], including active inertia/damping power, active phase jump power, and voltage jump reactive power [2]. While the amount of injected power quantifies how well GFM converters support the grid, the response speed is equally critical, as it determines how fast the capability is actually provided. Accordingly, fast fault current injection has been explicitly identified as a required GFM capability [2].

Minshen Lin, Li Zhang, and Qichen Yang are with the School of Electrical and Power Engineering, Hohai University, Nanjing 211100, China. Diaa Eldin A. Mansour is with the Electrical Power Engineering Department, Faculty of Engineering, Egypt-Japan University of Science and Technology, New Borg El-Arab City, Alexandria 21934, Egypt, and also with the Electrical Power and Machines Engineering Department, Faculty of Engineering, Tanta University, Tanta 31511, Egypt. Ahmed F. Zobaa is with the College of Engineering, Design and Physical Sciences, Brunel University of London, Uxbridge, UB8 3PH, UK. (Corresponding author: Li Zhang, e-mail: zhanglinuaa@hhu.edu.cn)

This work is supported in part by the National Key Research and Development Program of China under Grant 2024YFB2408600, in part by the National Natural Science Foundation of China under Grant 52322705, and in part by the special fund of Jiangsu Province for the Transformation of Scientific and Technological Achievements under Grant BA2023108.

Fast fault current injection on the millisecond timescale can benefit grid operation in many ways. Upon a grid voltage sag, rapidly injecting the predominantly reactive fault current can swiftly sustain voltages at the point of common coupling and in neighboring zones [3]. This shortens the duration of deep sags, helping nearby loads, especially motors and voltage-sensitive devices, to remain in service and avoid stalling or secondary collapse. Likewise, fast current injection enables faster voltage recovery after fault clearance, preventing undervoltage protection from triggering. Besides, promptly making the fault current signal available to protection relays can generally enhance protection responsiveness and selectivity [3].

The response time of GFM converters under grid disturbances has been addressed in grid codes and the literature. When the grid voltage falls below a threshold (e.g., 0.9 p.u.), GFM converters are expected to commence supplying reactive current within 5 ms [2], or to maintain a nearly constant internal voltage source to provide instantaneous fault current and power within a sub-cycle timeframe [4]. Importantly, for systems with 100% penetration of GFM converters, delivery of fault current within the first quarter of a fundamental cycle (i.e., 5 ms) has been identified as essential for stable grid operation [3]. Additionally, [5] demonstrated that with the proposed fault-ride-through strategy, reactive power can be fully injected within 5 ms following a grid voltage sag. Nevertheless, despite these findings, the impact of circuit and control parameters on the response time remains unclear, and under fixed control structures, a stringent 5 ms response time may not always be achievable across all grid conditions. This highlights the need for more detailed analytical studies to assess the feasibility and limitations of achieving the desired response time under various operating conditions.

To comprehensively evaluate the response of GFM converters under voltage sags, this letter proposes an analytical analysis of the key parameters governing the response time. First, a reduced-order model is developed to capture the system dynamics accurately. With this model, the closed-form solution for the response time is derived using the geometric singular perturbation method. Notably, it is shown that, across a wide range of grid conditions, the response time has an inherent limit of a quarter of the fundamental cycle, i.e., 5 ms. This limit can be approached by increasing the voltage-loop integral gain. However, an excessively large integral gain will induce small-signal instability. Thus, a control strategy that augments transient reactive current is proposed to approach and even break this limit while ensuring stability. Moreover, it is derived that the analytical response time constitutes an upper bound on the practical response time with current limiting. Based on

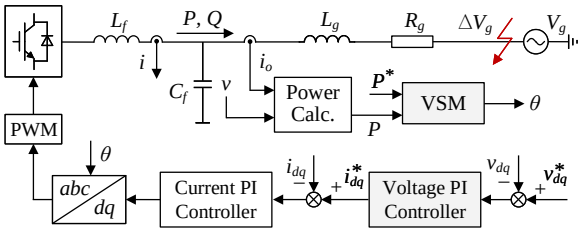

Fig. 1. System diagram of a grid-connected grid-forming converter.

the findings, potential refinements to grid code requirements regarding response time are discussed. The results are verified by hardware-in-the-loop (HIL) testing.

II. Modeling of Transient Dynamics

The diagram of the studied system is shown in Fig. 1. The GFM control with the virtual synchronous machine (VSM) control for power synchronization and cascaded voltage-current loops is adopted in this letter [6]. The inner voltage loop tracks the voltage reference, and the current loop enables rapid current regulation while limiting the fault current [7]. The GFM converter has an output LC filter, in connection to the grid through a series grid impedance.

Since the current loop is designed with a high bandwidth around 1/10 of the switching frequency f_{sw}, the output current can rapidly track its reference, with a time constant of 159 μs for 10 kHz f_{sw}. For transient dynamics on the millisecond timescale, the output current can be assumed to ideally track its reference without loss of accuracy. Thus, the system dynamics can be modeled with (i) the synchronization control, (ii) the voltage loop, and (iii) the circuit equations. The VSM control [1] emulates the dynamics of a synchronous machine by

$$\begin{cases} \dfrac{d\delta}{dt} = \omega - \omega_0 \\ \dfrac{d\omega}{dt} = \dfrac{\omega_0}{2H}(P^* - P) - \dfrac{D_p}{2H}(\omega - \omega_0) \end{cases}, \tag{1}$$

where δ is the rotor angle, defined as the phase difference between the voltage of the GFM converter and the grid, ω is the angular frequency, ω_0 is the nominal grid angular frequency, H is the inertia constant, and D_p is the damping coefficient. The active power reference P^* and the GFM converter output active power P are expressed in per unit (p.u.), with S_{base} as the base value. The voltage loop adopts proportional-integral (PI) control in the dq frame, and its output is the output current reference. Given that the output currents rapidly track their references, the voltage-loop control equations are given by

$$\begin{cases} \dfrac{dv_d}{dt} = -\dfrac{k_{iv}}{k_{pv}}(v_d - v_d^*) + \left(\dfrac{dv_d^*}{dt} - \dfrac{1}{k_{pv}}\dfrac{di_d}{dt}\right) \\ \dfrac{dv_q}{dt} = -\dfrac{k_{iv}}{k_{pv}}(v_q - v_q^*) + \left(\dfrac{dv_q^*}{dt} - \dfrac{1}{k_{pv}}\dfrac{di_q}{dt}\right) \end{cases}, \tag{2}$$

where $v_{d/q}$ are the dq components of the converter output voltage, $i_{d/q}$ are the dq components of the output current flowing through the filter inductor, and k_{pv} and k_{iv} are the proportional and integral gains of the voltage-loop PI controller, respectively. Besides, omitting the high-frequency ripple current through the filter capacitor, the output current dynamics are governed by the following circuit equations

$$\begin{cases} \dfrac{di_d}{dt} = \dfrac{1}{L_g}(v_d - v_g\cos\delta - R_g i_d + \omega L_g i_q) \\ \dfrac{di_q}{dt} = \dfrac{1}{L_q}(v_q + v_g\sin\delta - R_g i_q - \omega L_g i_d) \end{cases}, \tag{3}$$

where v_g is the grid voltage magnitude, L_g is the grid inductance, and R_g is the grid resistance.

By combining (1)-(3), the system dynamics can be described using only six state variables, $\mathbf{x} = [i_d, i_q, v_d, v_q, \omega, \delta]$, forming a reduced-order model (ROM) that can be solved with ordinary differential equation solvers. The accuracy of this model is assessed by comparison with full-order electromagnetic transient simulations carried out in MATLAB/Simulink, using a simulation time step of 1×10^{-6} s. The system for analysis has default parameters listed in Table I. The default active power reference and the voltage sag level are 0.5 p.u.; it will be shown in the subsequent section that the response time is

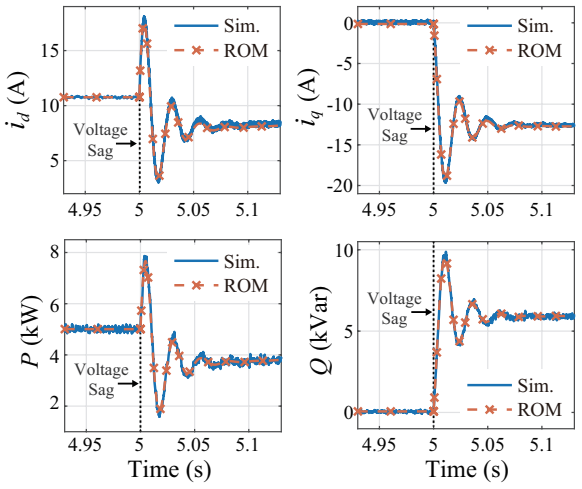

Fig. 2. Comparison of transient responses between the developed reduced-order model and the full-order electromagnetic simulation.

TABLE I
Default System Parameters

Symbol	Description	Value
S_{base}	Rated power	10 kVA
f_0	Grid frequency	50 Hz
V_{LL}	Grid line voltage	380 V
X/R	X/R ratio	5
SCR	Short circuit ratio	1.2
f_{sw}	Switching frequency	10 kHz
L_f	Filter inductance	2 mH
C_f	Filter capacitance	20 μF
H	Inertial constant	5 s
D_p	Damping coefficient	25 p.u.
k_{pv}	Voltage-loop P gain	0.08 A/V
k_{iv}	Voltage-loop I gain	100 A/Vs
k_{pi}	Current-loop P gain	5 V/A
k_{ii}	Current-loop I gain	100 V/As

independent of these parameters. As shown in Fig. 2, the ROM aligns with the simulation in equilibrium, and their transient responses during the voltage sag are also highly consistent. This consistency indicates that the ROM adequately captures the key parameters governing the system's transient dynamics. Besides, the low-pass-filtered reactive power can be used to regulate the voltage magnitude via droop control [1]. Since the filter time constant is much larger than that of the inner-loop dynamics, its effect on the analysis in the subsequent section is negligible and is therefore omitted.

It is worth noting that prior studies have developed analytical formulations for fault inrush current based on a voltage-source-behind-impedance assumption, which overlooks the fast control–circuit interaction that shapes the source voltage during disturbances [9], [10]. In contrast, the proposed ROM in this letter does not rely on this assumption; it preserves the coupled control-circuit impact in the time domain, which is critical for the accurate analytical characterization presented in the subsequent section.

III. Analytical Solution of Response Time

To analyze the response time, the grid voltage v_g is assumed to have a step of Δv_g at time t_0, causing the system to transition between equilibrium points $x_0 \to x_0'$. Since GFM converters inject predominantly reactive current under voltage sags, the response time is defined as the first instant such that i_q equals to its post-disturbance equilibrium value I'_{q0}, i.e.,

$$t_r := \min\{t \geq 0 \mid i_q(t+t_0) = I'_{q0}\}, \tag{4}$$

where $\min\{\cdot\}$ denotes minimum.

Given the high order and potentially separable time scales of the studied system, the geometric singular perturbation method is adopted to analytically solve the response time [8]. To facilitate the analysis, the current and voltage state vectors are separated from $\mathbf{x}$ as $\mathbf{i} = [i_d, i_q]^{\mathrm{T}}$ and $\mathbf{v} = [v_d, v_q]^{\mathrm{T}}$. By substituting (3) into (2), the state equations of current and voltage can be written in the following block-matrix form as

$$\begin{cases} \dot{\mathbf{i}} = A_{ii}\mathbf{i} + A_{iv}\mathbf{v} + \mathbf{u}_i \\ \dot{\mathbf{v}} = A_{vi}\mathbf{i} + A_{vv}\mathbf{v} + \mathbf{u}_v \end{cases}, \tag{5}$$

where the state matrices are

$$\begin{aligned} A_{ii} &= \begin{bmatrix} -1/\tau_i & \omega_0 \\ -\omega_0 & -1/\tau_i \end{bmatrix}, \quad A_{iv} = \frac{1}{L_g} I_{2\times 2}, \\ A_{vi} &= -\frac{1}{k_{pv}} A_{ii}, \qquad\qquad A_{vv} = -\frac{1}{\tau_v} I_{2\times 2}, \end{aligned} \tag{6}$$

and the input vectors are

$$\begin{aligned} \mathbf{u}_i &= \left[-\frac{v_g}{L_g}\cos\delta, \frac{v_g}{L_g}\sin\delta \right]^T, \\ \mathbf{u}_v &= \left[\frac{k_{iv}}{k_{pv}} v_d^* + \frac{v_g \cos\delta}{k_{pv} L_g}, \frac{k_{iv}}{k_{pv}} v_q^* - \frac{v_g \sin\delta}{k_{pv} L_g} \right]^T. \end{aligned} \tag{7}$$

Since the time dependence of $\mathbf{u}$ after grid disturbances is shaped by the outer loop through δ and v_d^* on a much slower timescale [7], the inner-loop current-voltage dynamics can therefore be analyzed using (5). The time constants $\tau_i = L_g/R_g$ and $\tau_v = k_{pv}/(k_{iv} + 1/L_g)$ determines the dynamics of $\mathbf{i}$ and $\mathbf{v}$, respectively, when the coupling terms A_{iv} and A_{vi} are negligible. Given that k_{pv} is typically designed such that $R_g \ll 1/k_{pv}$ [6], it follows that $\tau_i \gg \tau_v$, and the system can be partitioned into a slow current subsystem and a fast voltage subsystem. Consequently, the system dynamics can be solved through timescale separation using the geometric singular perturbation method. By introducing a small parameter $\varepsilon = \tau_v \ll 1$, the fast voltage dynamics can be rewritten as

$$\varepsilon \dot{\mathbf{v}} = -\mathbf{v} + \varepsilon A_{vi}\mathbf{i} + \varepsilon \mathbf{u}_v. \tag{8}$$

The attracting slow manifold for $\mathbf{v}$ can be parameterized by an affine graph up to first order in ε as

$$\mathbf{v} = h(\mathbf{i}; \varepsilon) = \varepsilon (M\mathbf{i} + \mathbf{m}) + O\left(\varepsilon^2\right), \tag{9}$$

where $M \in \mathbb{R}^{2\times 2}$ and $\mathbf{m} \in \mathbb{R}^2$. Substituting (9) into (8) yields

$$\varepsilon D_{\mathbf{i}} h(\mathbf{i}; \varepsilon)\, \dot{\mathbf{i}} = -\varepsilon (M\mathbf{i} + \mathbf{m}) + \varepsilon A_{vi}\mathbf{i} + \varepsilon \mathbf{u}_v + O\left(\varepsilon^2\right), \tag{10}$$

where $D_{\mathbf{i}}$ denotes differentiation with respect to $\mathbf{i}$. Substituting $D_{\mathbf{i}} h(\mathbf{i}; \varepsilon) = \varepsilon M$ and (5) into (10) gives

$$\varepsilon D_{\mathbf{i}} h(\mathbf{i}; \varepsilon)\, \dot{\mathbf{i}} = O(\varepsilon^2). \tag{11}$$

By matching the left and right sides of (10) order-by-order in ε and considering that the identity holds for all $\mathbf{i}$, the following relation can be obtained,

$$0 = \varepsilon(A_{vi} - M)\mathbf{i} + \varepsilon(\mathbf{u}_v - \mathbf{m}) \Rightarrow \begin{cases} M = A_{vi} \\ \mathbf{m} = \mathbf{u}_v \end{cases}. \tag{12}$$

Therefore, the solution of $\mathbf{v}$ is

$$\mathbf{v} = \varepsilon (A_{vi}\mathbf{i} + \mathbf{u}_v) + O\left(\varepsilon^2\right). \tag{13}$$

Substituting (13) into the slow current subsystem in (5) yields the first-order reduced slow system,

$$\dot{\mathbf{i}} = A_s\mathbf{i} + \mathbf{u}_s + O(\varepsilon^2), \tag{14}$$

where $A_s = A_{ii} + \varepsilon A_{iv}A_{vi}$ and $\mathbf{u}_s = \mathbf{u}_i + \varepsilon A_{iv}\mathbf{u}_v$ are the equivalent state matrix and input vector of the slow current subsystem that includes the first-order fast voltage dynamics, capturing the full-system dynamics within the time scale of interest. The detailed expression of A_s is

$$A_s = \left(1 - \frac{1}{1 + L_g k_{iv}}\right) \begin{bmatrix} -R_g/L_g & \omega_0 \\ -\omega_0 & -R_g/L_g \end{bmatrix}, \tag{15}$$

and the eigenvalues of A_s are

$$\lambda_s^{\pm} = \frac{1}{\tau_s} \pm j\omega_s = \left(1 - \frac{1}{1 + L_g k_{iv}}\right)\left(-\frac{R_g}{L_g} \pm j\omega_0\right). \tag{16}$$

To analyze the system under voltage sags, suppose the input $\mathbf{u}_s$ has a step at $t = t_0$, and the corresponding post-step equilibrium is given by $\mathbf{i}_e = -A_s^{-1}\mathbf{u}_s(t_0^+)$. A new state variable $\tilde{\mathbf{i}} := \mathbf{i} - \mathbf{i}_e$ is introduced to describe the oscillatory mode excited by the effective initial deviation $\tilde{\mathbf{i}}(t_0) = A_s^{-1}\left[\mathbf{u}_s(t_0^+) - \mathbf{u}_s(t_0^-)\right]$: in case of Δv_g, this deviation is

$$\tilde{\mathbf{i}}(t_0) = \frac{-\Delta v_g/L_g}{(R_g/L_g)^2 + \omega_0^2} \begin{bmatrix} \omega_0 \sin\delta_0 - (R_g/L_g)\cos\delta_0 \\ \omega_0 \cos\delta_0 + (R_g/L_g)\sin\delta_0 \end{bmatrix}. \tag{17}$$

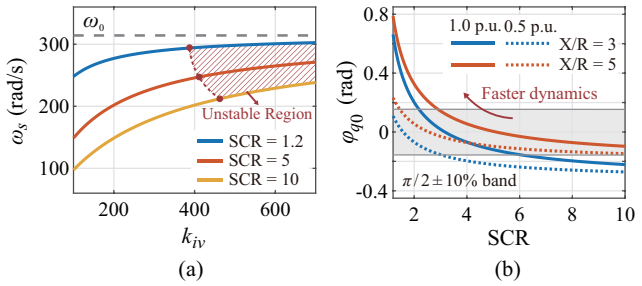

Fig. 3. Impact of parameters on ω_s and φ_{q0}.

Thus, the effective current system equation is

$$\dot{\tilde{\mathbf{i}}} = A_s \tilde{\mathbf{i}}, \tag{18}$$

and the solution of (18) is given by

$$\tilde{\mathbf{i}}(t) = e^{A_s(t-t_0)} \tilde{\mathbf{i}}(t_0). \tag{19}$$

This solution can be expanded via eigen-decomposition as

$$\tilde{\mathbf{i}}(t) = \mathbf{r}_s \mathbf{w}_s^{\mathrm{T}} \tilde{\mathbf{i}}(t_0) e^{\lambda_s^+(t-t_0)} + \overline{\mathbf{r}_s \mathbf{w}_s^{\mathrm{T}}} \tilde{\mathbf{i}}(t_0) e^{\lambda_s^-(t-t_0)}, \tag{20}$$

where $\mathbf{r}_s = [1, j]^{\mathrm{T}}$, $\mathbf{w}_s^{\mathrm{T}} = \frac{1}{2}[1, -j]$, and their complex conjugates are the right and left eigenvectors with respect to $\lambda_s^{\pm}$. Thus, the effective reactive current can be computed by

$$\tilde{i}_q(t) = [0, 1] \cdot \tilde{\mathbf{i}} = 2|K_q| e^{-\frac{t-t_0}{\tau_s}} \cos\left[\omega_s(t-t_0) + \varphi_{q0}\right], \tag{21}$$

where the complex modal coefficient and initial phase are

$$K_q = [0, 1] \cdot \mathbf{r}_s \mathbf{w}_s^{\mathrm{T}} \tilde{\mathbf{i}}(t_0), \qquad \varphi_{q0} = \arg K_q. \tag{22}$$

Under (4), the response time can be computed by

$$2|K_q| e^{-\frac{t-t_0}{\tau_s}} \cos\left[\omega_s(t-t_0) + \varphi_{q0}\right] = 0, \tag{23}$$

and the solution is

$$t_r = \frac{\pi/2 - \varphi_{q0}}{\omega_s}, \tag{24}$$

where the initial phase φ_{q0} is given by

$$\varphi_{q0} = \tan^{-1}\left[\frac{\omega_0 \sin\delta_0 - (R_g/L_g)\cos\delta_0}{\omega_0 \cos\delta_0 + (R_g/L_g)\sin\delta_0}\right]. \tag{25}$$

It follows from (24) that the response time is determined by both the dominant frequency ω_s and the initial phase φ_{q0}. From (16), ω_s has an inherent limit of the fundamental frequency ω_0: in weaker grids and with larger voltage-loop integral gains, ω_s approaches ω_0. Fig. 3(a) shows how ω_s varies with SCR and k_{iv}: in stronger grids, a larger k_{iv} is required for ω_s to approach ω_0, whereas an excessively large k_{iv} induces small-signal instability as stability margin declines. Fig. 3(b) shows that φ_{q0} decreases with SCR and X/R ratio, and increases with P^*. Notably, φ_{q0} falls within $\pm 10\%$ band of $\pi/2$ at zero phase for a wide range. Therefore, the response time is primarily limited by the dominant frequency, and the impact of φ_{q0} becomes more pronounced in weaker grids, with higher X/R ratios, or larger active-power setpoints.

Likewise, the above procedures can be applied to solve the analytical solution of the response time under grid phase jump disturbances. As GFM converters will naturally inject or absorb active phase jump power [2] when the grid phase

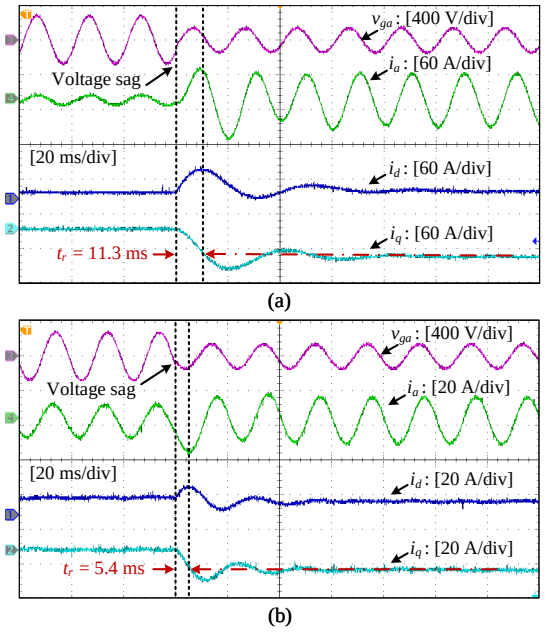

Fig. 4. Response curves under voltage sags. (a) SCR = 5; (b) SCR = 1.2.

changes, in this case, the active current response time is analyzed. By adopting a different effective initial deviation in (17), the response time under a grid phase jump of $\Delta\delta$ is

$$t_r^{\Delta\delta} = \frac{-\pi/2 - \varphi_{d0}^{\Delta\delta}}{\omega_s}, \tag{26}$$

and the initial phase is

$$\varphi_{d0}^{\Delta\delta} = \tan^{-1}\left[\frac{(R_g/L_g)\cos\bar{\delta}_0 - \omega_0 \sin\bar{\delta}_0}{(R_g/L_g)\sin\bar{\delta}_0 + \omega_0 \cos\bar{\delta}_0}\right] - \pi, \tag{27}$$

where $\bar{\delta}_0 = \delta_0 + \Delta\delta/2$. It is worth noting that promptly providing the active phase jump power facilitates the rapid initiation of the synchronization process in the GFM converter. Since synchronization control of VSM is typically characterized by a time constant on the order of hundreds of milliseconds, detailed investigation is left for future work.

In addition, in GFM converter systems, the closed-loop control dynamics typically evolve on a fast time scale, whereas the circuit dynamics evolve on a slow time scale. Therefore, the response-time analysis in this section is extendable beyond the cascaded inner-loop control in the rotating reference frame. For other types of controllers, e.g., cascaded controllers in the stationary reference frame, single-loop voltage controllers, and model predictive voltage controllers, once the inner-loop dynamics are formulated, the same reduced-order modeling and geometric singular perturbation procedure can be applied to analytically characterize the response time. Besides, in parallel multi-converter systems, it can be derived that the equivalent grid impedance seen by each converter is increased. By precisely evaluating the equivalent impedance, the analytical expression for quantifying the response time remains applicable.

IV. Hardware-in-the-Loop Verification

To validate the analytical expression for the response time derived in the previous section, HIL tests are carried out.

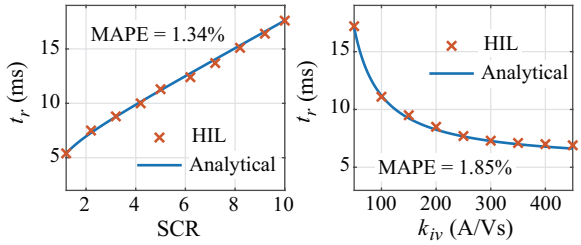

Fig. 5. Accuracy evaluation of the analytical expression.

Fig. 4(a) shows the system responses following a grid voltage sag to 0.5 p.u. with an SCR of 5. The measured response time is 11.3 ms, which closely matches the analytical value t_r = 11.2 ms given by (24). For a smaller SCR of 1.2, Fig. 4(b) presents faster responses as predicted by (24), and the measured response time is 5.4 ms, again in close agreement with the analytical t_r of 5.39 ms.

To evaluate the accuracy of the analytical expression more comprehensively, another set of HIL tests is conducted. Fig. 5 illustrates how t_r changes as SCR (equivalently, the grid inductance L_g) and k_{iv} are continuously varied, while all other parameters are held at their default values. In both cases, the measured data closely match the analytical predictions, with mean absolute percentage errors (MAPEs) below 2%, demonstrating the high accuracy of the analytical response time across a wide range of system parameters.

Moreover, given that t_r can be significantly longer than a quarter of the cycle in non-weak grids, a transient reactive current augmentation (TRCA) strategy is proposed to further accelerate the response. This strategy is motivated by the fact that, according to (24), t_r is independent of the severity of the voltage sag. Under a deeper voltage sag, the post-disturbance equilibrium reactive current is larger, and thus a higher ramp rate of i_q is required to achieve the same response time. Therefore, by adjusting the reactive voltage reference to emulate a deeper sag at the early stage of the disturbance, i_q can have a steeper initial ramp rate, enabling a shorter time to reach its post-disturbance equilibrium value. Since the

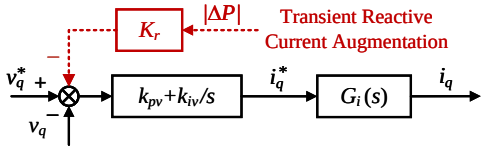

Fig. 6. Block diagram of the transient reactive current augmentation strategy.

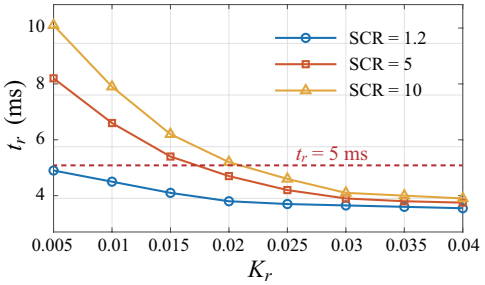

Fig. 7. Impact of K_r on the response time under various grid strengths.

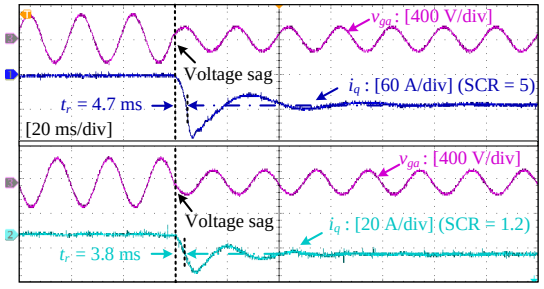

Fig. 8. Expedited response with transient reactive current augmentation.

active power deviates from its reference during the transient, $K_r|\Delta P|$ is chosen to emulate the additional voltage sag for half of a fundamental cycle and thereby augments the transient reactive current, as shown in Fig. 6. A parametric evaluation shown in Fig. 7 quantifies the impact of K_r on the response time, demonstrating that increasing K_r consistently shortens the response time across a wide range of grid strengths. Nevertheless, an excessively large K_r can induce oscillations and diminish the effective reactive current, thereby limiting the voltage-support capability. Considering this trade-off, K_r = 0.02 is selected to achieve a fast response (approximately $\leq$5 ms) with acceptable damping. With TRCA, the response curves are shown in Fig. 8. Compared to Fig. 4, the response time for SCR = 5 is reduced to 4.7 ms, and for SCR = 1.2, it is reduced to 3.8 ms, demonstrating the effectiveness of this strategy in stably approaching and breaking the inherent limit imposed by the fundamental frequency.

In practice, current limiting control is adopted in GFM converters to limit the overcurrent, typically via virtual impedance and circular current limiter [11]–[13]. Both methods impose an upper bound $I_{\max}$ on the output current, but their implications for the response time are distinct.

• **Virtual impedance**. Virtual impedance is activated when the current reaches a predefined threshold $I_{\text{th}} < I_{\max}$. It acts by subtracting the virtual voltage drop from the voltage reference, thereby increasing the effective output impedance. According to the response-time analysis in Sec. III, increasing the output impedance effectively reduces the SCR, leading to accelerated response. Figure 9 shows the response curves with designed adaptive virtual impedances of X/R = 5 that limit $I_{\max}$ to 3 p.u. and 1.5 p.u. in case of bolted fault, respectively. Compared with the response without current limiting in Fig. 4(a), virtual impedance yields a shorter response time, and a larger virtual impedance (corresponding to a smaller $I_{\max}$) further reduces both the magnitude of the post-disturbance current and the response time.

• **Circular current limiter**. With a circular limiter, saturation is triggered when $|i^*| > I_{\max}$, yielding saturated current reference

$$i^*_{\text{sat}} = \begin{cases} i^*, & |i^*| \leq I_{\max} \\ \dfrac{I_{\max}}{|i^*|}\, i^*, & |i^*| > I_{\max} \end{cases}, \tag{28}$$

where i^* is the unsaturated current reference. When PI/PR voltage controllers are used, standard anti-windup schemes

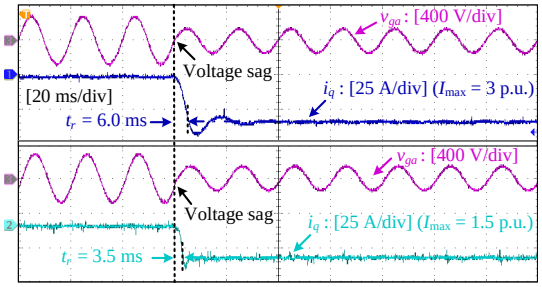

Fig. 9. Response curves with adaptive virtual impedance (SCR = 5).

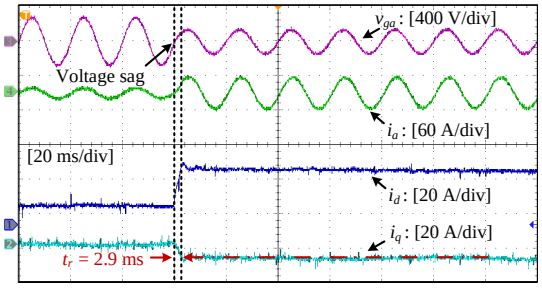

Fig. 10. Response curves with circular current limiter (SCR = 5).

(e.g., integrator clamping or back-calculation) effectively suppress the integral action during saturation, which can be interpreted as introducing a variable virtual resistance $R_v = |i^*|/(I_{\max} k_{pv})$ in the output impedance [14]. Since the integral contribution is suppressed ($k_{iv} \to 0$) during current limiting, according to (16), the oscillating frequency reduces to ω_0 and the decaying time constant becomes

$$\tau_s = -\frac{L_g}{R_g + R_v}. \tag{29}$$

Given that $|i^*|/I_{\max} > 1$, R_v is lower bounded by $1/k_{pv}$, and thus τ_s is upper bounded by τ_s^{ub} = 0.69 ms for SCR = 5 and k_{pv} = 0.08 A/V. Therefore, the response time to reach 99% of the post-disturbance equilibrium value is $-\tau_s \ln(0.01)$, which is smaller than $-\tau_s^{\text{ub}} \ln(0.01)$ = 3.18 ms. As shown in Fig. 10, the response time under voltage sags with a circular current limiter is 2.9 ms, which is below the derived bound, and the oscillating mode of ω_0 is suppressed, validating that the fast-decaying mode is the dominant mode during the transient.

In sum, the analytical response time in (24) constitutes an upper bound on the practical response time with current limiting. Besides, grid specifications are evolved to require GFM converters to provide substantial short-term overload capability (e.g., 3 p.u. for 10 s). In many disturbance scenarios, such overload capability implies that current limiting may not be triggered. Therefore, the analytical results in this letter are broadly applicable across a wide range of operating conditions.

The above results motivate a re-examination of grid code requirements for the response time of GFM converters. One possible refinement is to specify the response time for different grid strengths, rather than enforcing a fixed value. For each grid strength, once operating scenarios involving P^* and X/R ratios are identified, the lowest initial phase is determined, and the corresponding maximum response time, with appropriate margins, can be adopted as the grid-code requirement.

V. Conclusion

This letter presents an analytical analysis of the key parameters influencing the response time of GFM converters. By developing an ROM, the analytical solution and limits of the response time are derived, and a control strategy that augments transient reactive current is proposed to further accelerate the response. Moreover, it is derived that the analytical response time constitutes an upper bound on the practical response time with current limiting. The results are verified by HIL testing.

References

[1] H. Wu, X. Wang, and L. Zhao, "Design Considerations of Current-Limiting Control for Grid-Forming Capability Enhancement of VSCs Under Large Grid Disturbances," IEEE Transactions on Power Electronics, vol. 39, no. 10, pp. 12081–12085, Oct. 2024.

[2] National Grid ESO, "GC0137: Minimum specification required for provision of GB grid forming (GBGF) capability," London, U.K., Nov. 2021.

[3] ENTSO-E, "High penetration of power electronic interfaced power sources and the potential contribution of grid forming converters," Brussels, Belgium, 2020.

[4] AEMO, "Voluntary specification for grid-forming inverters," Australia, May 2023.

[5] R. Rosso, S. Engelken, and M. Liserre, "On The Implementation of an FRT Strategy for Grid-Forming Converters Under Symmetrical and Asymmetrical Grid Faults," IEEE Transactions on Industry Applications, vol. 57, no. 5, pp. 4385–4397, Sep. 2021.

[6] Y. Li, Y. Gu, Y. Zhu, A. Junyent-Ferre, X. Xiang, and T. C. Green, "Impedance Circuit Model of Grid-Forming Inverter: Visualizing Control Algorithms as Circuit Elements," IEEE Transactions on Power Electronics, vol. 36, no. 3, pp. 3377–3395, Mar. 2021.

[7] F. Zhao, T. Zhu, Z. Li, and X. Wang, "Low-Frequency Resonances in Grid-Forming Converters: Causes and Damping Control," IEEE Transactions on Power Electronics, vol. 39, no. 11, Nov. 2024.

[8] N. Fenichel, "Geometric singular perturbation theory for ordinary differential equations," Journal of Differential Equations, vol. 31, no. 1, 1979.

[9] B. Cui, L. Huang, P. C. Loh and F. Blaabjerg, "A Hybrid Transient Virtual Resistor Method for Restraining Transient Overcurrent of Grid-Forming Inverter During Grid Fault and Postfault Recovery," IEEE Transactions on Industrial Electronics, 2026.

[10] Z. Shuai, W. Huang, C. Shen, J. Ge and Z. J. Shen, "Characteristics and Restraining Method of Fast Transient Inrush Fault Currents in Synchronverters," IEEE Transactions on Industrial Electronics, vol. 64, no. 9, pp. 7487-7497, Sept. 2017.

[11] B. Fan, T. Liu, F. Zhao, H. Wu and X. Wang, "A Review of Current-Limiting Control of Grid-Forming Inverters Under Symmetrical Disturbances," IEEE Open Journal of Power Electronics, vol. 3, pp. 955-969, 2022.

[12] N. Baeckeland, D. Chatterjee, M. Lu, B. Johnson and G. -S. Seo, "Overcurrent Limiting in Grid-Forming Inverters: A Comprehensive Review and Discussion," IEEE Transactions on Power Electronics, vol. 39, no. 11, pp. 14493-14517, Nov. 2024.

[13] X. He, M. A. Desai, L. Huang and F. Dörfler, "Cross-Forming Control and Fault Current Limiting for Grid-Forming Inverters," IEEE Transactions on Power Electronics, vol. 40, no. 3, pp. 3980-4007, March 2025.

[14] B. Fan and X. Wang, "Equivalent Circuit Model of Grid-Forming Converters With Circular Current Limiter for Transient Stability Analysis," IEEE Transactions on Power Systems, vol. 37, no. 4, pp. 3141-3144, July 2022.